Research Square

Preprints are preliminary reports that have not undergone peer review.
They should not be considered conclusive, used to inform clinical practice,
or referenced by the media as validated information.

Selective electrocatalytic hydrogenation of bio-oil to oxygenated chemicals via suppression of deoxygenation

Tao Peng
University of Toronto https://orcid.org/0000-0001-8517-5368
Taotao Zhuang
University of Toronto
Yu Yan
University of Toronto
Jin Qian
Lawrence Berkeley National Laboratory
Graham Dick
Ecole Polytechnique Fédérale de Lausanne
Jean Behaghel de Bueren
Ecole Polytechnique Fédérale de Lausanne
Sung-Fu Hung
University of Toronto
Ziyun Wang
University of Toronto https://orcid.org/0000-0002-2817-8367
Joshua Wicks
University of Toronto https://orcid.org/0000-0001-7819-1167
F. Pelayo Garcia De Arquer
University of Toronto
Jehad Abed
University of Toronto https://orcid.org/0000-0003-1387-2740
Ning Wang
University of Toronto
Armin Rasouli
University of Toronto
Geonhui Lee
University of Toronto https://orcid.org/0000-0002-9264-7420
Miao Wang
Shenzhen University
Daping He

Hubei Engineering Research Center of RF-Microwave Technology and Application, Wuhan University of Technology

Zhe Wang
Wuhan University of Technology

Zhixiu Liang
Brookhaven National Laboratory

Liang Song
Brookhaven National Laboratory

Xue Wang
University of Toronto https://orcid.org/0000-0002-6298-1858

Bin Chen
University of Toronto

Adnan Ozden
University of Toronto

Yanwei Lum
University of Toronto

Wan Ru Leow
University of Toronto

Mingchuan Luo
Department of Electrical and Computer Engineering, University of Toronto, 10 King's College Road, Toronto, ON M5S 3G4, Canada.

Déboa Meira
Canadian Light Source https://orcid.org/0000-0002-7529-2736

Alexander Ip
University of Toronto

Jeremy Luterbacher
EPFL https://orcid.org/0000-0002-0967-0583

Wei Zhao
Shenzhen University

Edward Sargent (ted.sargent@utoronto.ca)
University of Toronto https://orcid.org/0000-0003-0396-6495

Article

Keywords: electrocatalytic hydrogenation, catalysis

Posted Date: January 18th, 2021

DOI: https://doi.org/10.21203/rs.3.rs-131880/v1

License: This work is licensed under a Creative Commons Attribution 4.0 International License.
Read Full License

Abstract

Catalytic hydrogenation of bio-oil provides an avenue to produce renewable chemicals. To this end, electrocatalytic hydrogenation is especially interesting when powered using low-carbon electricity; however, it has to date lacked the needed selectivity: when hydrogenating bio-oil to oxygenated hydrocarbons, for example, it reduces the desired oxygenated groups (-OH and -OCH_3). Here we report that Rh and Au modulate electronic structure of Pt and steer intermediate energetics to favor the hydrogenation while suppressing deoxygenation using computational studies and in-situ spectroscopies. PtRhAu catalysts achieve a record 47% faradaic efficiency (FE) and a partial current density (J_p) of 28 $mA{\cdot}cm^{-2}$ toward oxygenated 2-methoxycyclohexanol from lignin-derived guaiacol under room temperature and ambient pressure, representing 1.5x FE and 3.5x J_p increases compared to the best prior reports. We further demonstrate an integrated lignin biorefinery where wood-derived lignin oils are selectively hydrogenated and funneled to the oxygenated 2-methoxy-4-propylcyclohexanol using PtRhAu catalysts.

Introduction

Biomass-derived bio-oil containing lignin-derived aromatic hydrocarbons is potential alternatives to fossil feedstocks in chemical production[1-5]. Unlocking this potential will benefit from progress in the selective hydrogenation of lignin-derived aromatic monomers to oxygen-functionalized chemical motifs – building-blocks of pharmaceuticals, natural products, and agricultural chemicals – under gentle conditions, such as in scalable systems functioning at or near ambient pressures and at modest temperatures[6-10].

Thermocatalytic hydrogenation has been widely studied for the valorization of lignin monomers[11,12]. Thermocatalytic hydrogenation is an energy-intensive process conducted at high reaction temperatures (~100-500^oC) and hydrogen pressures (~1-200 bar), necessary because of the stable pi bonds of aromatic rings[13]. Unfortunately, present-day thermocatalytic hydrogenation methods have so far led to the deoxygenation of lignin monomers (i.e. they reduce oxygenated functional groups, OFGs) producing partially or completely deoxygenated products (e.g. phenol, cyclohexanol, and cyclohexane)[12,14-17]. For this reason, the production of OFG-rich hydrocarbons has required a multiple-step process of hydrogenation and oxidation[12,18].

One-step hydrogenation of lignin monomers, if it selectively retains the needed OFGs characteristic of lignin precursors, would reduce the number of chemical steps and appeal to the chemical industry due to the reduced carbon footprint of lignin monomers compared to petroleum-derived feedstocks[4,19,20].

Here we selectively hydrogenate lignin monomers: we are able to retain the original OFGs in a one-step aqueous electrocatalytic hydrogenation (ECH) process. The ECH of biomass benefits from mild operating conditions (ambient temperature and pressure), avoids organic solvents and H_2, and offers routes to tune

product selectivity[21,22]. Moreover, Pt-based heterogeneous catalysts prefer the production of cis isomers[23].

A key difficulty in an electrocatalytic approach is that deoxygenation is thermodynamically favored in the cathodic, reducing, and electron-rich environment[10,16,24,25]. As a result, high FE and current density toward OFG-rich products are challenging to achieve – a factor further compounded by the competing hydrogen evolution reaction[10].

We sought therefore a route to develop new electrocatalysis with high selectivity in mind. We selected metals that would modulate the electronic properties of Pt, addressing the energetics of key reaction intermediates to achieve these goals simultaneously. Using the resultant new electrocatalysts, we selectively hydrogenate lignin monomers (i.e. guaiacol and syringol with OFGs such as -OH and -OCH_3) to OFG-rich chemicals at room temperature and ambient pressure. The oxygenated 2-methoxycyclohexanol (2MC) from guaiacol (Fig. 1a) and syringol is an OFG-rich intermediate for pharmaceutical compounds (i.e., β-lactam antibiotics for HIV)[26] and synthetic perfumes[27].

We further demonstrate the versatility of PtRhAu catalysts in an integrated lignin biorefinery to obtain oxygenated chemicals directly from lignocellulosic biomass. We first converted birch wood to lignin-derived oils containing 4-propylsyringol (4PS) and/or 4-propylguaiacol (4PG) using aldehyde-assisted fractionation (AAF) followed by hydrogenolysis[5,28]. These lignin-derived oils were then selectively hydrogenated and funneled to a single OFG-rich chemical 2-methoxy-4-propylcyclohexanol for synthetic perfumes using our novel electrocatalysts under ambient conditions.

Results

Density functional theory (DFT) calculations We began by screening a range of single-metal catalysts (Pt, Rh, Au, Ag, Ni, Pd, Cu, Ru, and Ir) (Fig. 1b, Figs. S1-S3, and Tables S1-S3). DFT calculations reveal that an increase in the guaiacol adsorption energy ($E_{ad\text{-}G}$) is closely linked to an increased partial current density toward 2MC (Fig. 1b). This preliminary study highlighted Pt ($E_{ad\text{-}G}$ = 2.12 eV) and Rh ($E_{ad\text{-}G}$ = 2.67 eV) as potential candidates due to their high adsorption energies for guaiacol (Fig. 1b). We then moved on to binary systems, modulating Pt with Rh (20% atomic concentration for optimized PtRh) to simultaneously increase the adsorption energy of guaiacol and current density toward 2MC.

To suppress the undesired loss of OFGs, we sought to avoid the reduction of the C-OCH_3 bond, which is more prone to scission than C-OH (Fig. S4). We reduced the C-OCH_3 bond length on the catalyst surface by modulating PtRh using a third transition metal. Our DFT calculations indicate that Au (with an adsorbed guaiacol C-OCH_3 bond length of 1.360 Å) has a stronger ability to localize the σ-electron and reduce the C-OCH_3 bond length compared to Pt (bond length = 1.365 Å), Rh (bond length = 1.378 Å), and other selected metals (Table S1). We predicted, therefore, that it would kinetically suppress the detachment of the -OCH_3 group. Combining the above two descriptors (adsorption energy of guaiacol and

C-OCH_3 bond length), we obtained a contour diagram (Fig. 1c) that suggests improved performance using ternary PtRhAu catalysts.

Next, with the goal of further understanding the mechanism, we calculated the surface reaction network and the energetics of the intermediates (Fig. 2a and Fig. S4). The energy profile (Fig. 2b) indicates that the rate-determining step along the ECH pathway is the addition of the first pair of hydrogen atoms. Both PtRh (1.64 eV) and PtRhAu (1.59 eV) catalysts lead to a decrease in hydrogenation energy compared to Pt alone (1.79 eV), indicating a synergistic role of Rh in hydrogenation (Fig. 2b). As for the undesired demethoxylation (Fig. 2c) and dehydroxylation (Fig. 2d) pathways, PtRhAu catalysts are thermodynamically less favorable than pure Pt, indicating that Au inhibits deoxygenation. Amongst Pt, PtRh, and PtRhAu, only the ternary PtRhAu catalysts have an ECH pathway (1.64 eV) that is more favorable than the demethoxylation pathway (1.82 eV). By comparing five elementary steps – some relating to the activity (adsorption, hydrogenation, desorption) and others to selectivity (demethoxylation and dehydrogenation) – we concluded that the ternary PtRhAu catalysts showed particular promise (Fig. 2e).

Catalyst synthesis and characterization. We synthesized PtRhAu (Fig. 3a) and relevant controls using an electrochemical deposition method (see Supplementary methods). Synchrotron X-ray diffraction (XRD) peaks of PtRhAu and PtRh (Fig. 3b) shift to lower and higher 2θ values than pure Pt, indicating the formation of PtRhAu and PtRh alloys. The PtRhAu alloy has a dendritic morphology consisting of nanoparticles with diameters of ~5 nm (Fig. 3c and Figs. S6-S8). The synchrotron XRD peak shifts, along with STEM and HRTEM images, indicate PtRhAu has a lattice expansion (lattice spacing of 2.29 Å, Figs. 3d and e) compared to Pt (2.26 Å), while PtRh has a lattice contraction (2.24 Å) (Fig. S7). We performed electron energy loss spectroscopy (EELS) elemental mapping and found a uniform spatial distribution of Pt, Au, and Rh in PtRhAu to within the 0.25 nm spatial resolution of the technique (Fig. 3f). We used inductively coupled plasma atomic emission spectroscopy (ICP-AES) to determine the molar ratio of Pt:Rh:Au, finding a ratio of 48:8:44 for an optimized PtRhAu catalyst with the most selective hydrogenation activity (Fig. S9).

Electrocatalytic hydrogenation performance. We characterized the ECH of guaiacol by performing linear sweep voltammetry (LSV) in a three-electrode H-cell system (Fig. 4) with (Fig. 4a) and without (Fig. S10) 120 mM guaiacol. We determined that the PtRhAu catalyst hydrogenates guaiacol between -0.05 and -0.2 V.

By optimizing the reaction conditions (Fig. S11), catalyst composition (Fig. S12), and current density (Fig. 4a and Fig. S13), we achieved a FE of 47 ± 1% and a partial current density of 28 ± 0.5 $mA{\cdot}cm^{-2}$ toward 2MC using the PtRhAu catalyst at -0.15 V (Fig. S14). ^1H NMR (Fig. S15) analyses confirm the production of 2MC from guaiacol by ECH at 60 $mA{\cdot}cm^{-2}$ after 1 hour. PtRhAu presents 1.3x and 4.7x increases in FE toward 2MC compared to PtRh (35 ± 1%) and Pt (10 ± 1%). The current density toward 2MC is 3.5x greater than the prior reports (7.95 $mA{\cdot}cm^{-2}$, Table S4) that used a Ru catalyst[29].

Tafel analysis of 2MC production from guaiacol by ECH gives the slopes of 100, 280, and 150 $mV \cdot dec^{-1}$ for PtRhAu, PtRh, and Pt respectively (Fig. 4c), indicating that ECH is improved with PtRhAu. Comparing the product distribution of PtRh and Pt (Fig. 4d and Fig. S16) indicates that incorporation of Rh increases selectivity toward 2MC without increasing the production of organic by-products, suggesting that Rh promotes the selective hydrogenation of guaiacol toward 2MC. With the further incorporation of Au, the ternary PtRhAu catalysts enable higher FE toward 2MC and suppresses the formation of deoxygenated by-products (methoxy-cyclohexane, cyclohexanone, and cyclohexanol) (Fig. 4d). The optimal PtRhAu catalyst converts 91% of the guaiacol with a 74% selectivity giving a 68% yield of 2MC (Fig. S17).

We found that PtRhAu catalyst provides a high stereoselectivity toward cis-2-methoxycyclohexanol with 99.5% selectivity (Fig. 4e and Figs. S18-S20). The preferential production of the thermodynamically unfavored cis isomer of 2MC on Pt-based electrocatalysts is an interesting result and distinct from the observations from thermocatalysis[23,30].

We explored the stability of the ternary catalysts by performing ECH on guaiacol at a constant current density of 60 $mA \cdot cm^{-2}$. The PtRhAu catalyst maintains a FE of over 40% toward 2MC at -0.15 V for over 12 hours of continuous operation (Fig. 4f). We also selectively hydrogenated the lignin monomer syringol (2,6-dimethoxyphenol) and retain one methoxy group ($-OCH_3$) to obtain the same product 2MC with a FE of 36% at a total current density of 60 $mA \cdot cm^{-2}$ (Fig. S21). This selective retention of one methoxy group provides potential to funnel wood-derived lignin monomer mixtures into a single product, which is demonstrated in later section using wood-derived lignin monomer mixtures.

Mechanistic investigations. By tracking changes in X-ray absorption near edge structure (XANES) and extended X-ray absorption fine structure (EXAFS) spectra (Figs. 5a-d), we were able to examine the local electronic and coordination structure of PtRhAu catalysts. XANES plots for Pt, Au, and Rh (Figs. 5a-c) reveal the metallic Pt, Au, and Rh phase in all samples, consistent with the results of X-ray photoelectron spectroscopy (XPS) (Fig. S22). We also investigated the catalyst stability during the ECH of guaiacol at a current density of 60 $mA \cdot cm^{-2}$ using *in-situ* XAS (Fig. S23). Pt/Au L_3-edge and Rh K-edge XANES of all the catalysts show no obvious change in the valence state of Pt, Au, and Rh during the ECH of guaiacol.

EXAFS spectra of the Rh K-edge for PtRhAu (Fig. 5d) reveal a significant change in atomic bonding of the Rh atom compared to pure Rh. PtRhAu and PtRh catalysts exhibit a decreased Rh-M (M = Pt, Au, and Rh) coordination number and an increased Rh-M interatomic distance (PtRhAu > PtRh > Rh) compared to pure Rh, suggesting the formation of a PtRhAu solid solution alloy [31]. This increased Rh-M interatomic distance is consistent with the lattice expansion observed using STEM and XRD (Fig. 3). Using *in-situ* EXAFS to investigate atomic bonding near the Rh atom of PtRh and PtRhAu catalysts (Fig. S24), we found no obvious changes in the Rh-M coordination number and interatomic distance, indicating that PtRhAu alloy structure is stable during the ECH of guaiacol.

We investigated the ECH mechanism by evaluating reaction intermediates using electrode potential-dependent *in-situ* Raman spectra (Fig. 5e) and *in-situ* infrared reflection-absorption spectroscopy (IRRAS)

(Fig. S25). We associate the characteristic peaks from 0 to -0.37 V versus RHE with the ECH of guaiacol. PtRhAu has a wider electrochemical potential window (0 to -0.37 V) compared to Pt (0 to -0.14 V) (Fig. S26). The *in-situ* Raman spectra of PtRhAu show intensive peaks associated with the adsorption (CCH wag, in-plan C-H bending, and C=C of aromatic ring)[32,33] and ECH (hydrogenation)[34] of guaiacol on catalyst surface, indicating a favorable ECH of guaiacol. The PtRhAu catalyst shows decreased intensity of peaks associated with C-O cleavage (C-O stretch and C-OCH_3 stretch)[33] in a potential range of 0 and -0.18 V compared to Pt (Fig. S26), indicating the suppression of deoxygenation. In contrast, Pt shows a strong peak located at 1161 cm^{-1} and evident deoxygenation at -0.09 V (Fig. S26). *In-situ* IRRAS of PtRhAu (Fig. S25) shows intense peaks related to the adsorption of guaiacol and 2MC product, along with suppressed peak related to C-O cleavage, confirming suppressed deoxygenation on PtRhAu catalyst surface.

Integrated lignin biorefinery to produce oxygen-functionalized chemicals from birch wood. We then sought to develop an integrated lignin valorization approach to upgrade birch wood to the oxygenated chemical 2-methoxy-4-propylcyclohexanol (**1**) – a value-added fragrance compound (Fig. 6a). By using AAF with propionaldehyde as the stabilizing aldehyde, we first fractionated the birch wood into cellulose-rich solids, dipropylxylose, and propionaldehyde stabilized lignin (Fig. 6b)[35]. The lignin was then hydrogenolyzed using a 5 wt% Ru/C catalyst in tetrahydrofuran (THF) to produce a complex solution consisting of lignin oligomers and monomers. After removing the catalyst by filtration, the concentrated solution was subjected to hydrodistillation to isolate the lignin monomers as a mixture (lignin-derived oil) of 66 mol% 4-propylsyringol (4PS) (**2**), 12 mol% 4-propylguaicol (4PG) (**3**), and 22 mol% concomitants (Fig. 6c and Fig. S29)[28].

This lignin-derived oil was then selectively hydrogenated to the oxygenated 2-methoxy-4-propylcyclohexanol (**1**, having -OH and -OCH_3 retained) with suppressed deoxygenation using PtRhAu catalyst. The PtRhAu catalyst shows superior performance on upgrading this lignin monomer mixture (Fig. 6c and Fig. S30 and S31), achieving a 68% selectivity (up to 72% when using purified lignin bio-oil containing wood-derived 92 mol% 4-propylsyringol, Fig. S35) toward the target product **1** at a 96% conversion rate during a 3-hour continuous reaction. The FE toward product **1** reaches 19% during the initial first hour of reaction with an applied current density of 20 $mA{\cdot}cm^{-2}$ (Fig. 6c).

Conclusion

By alloying Pt with Rh and Au, we realized ternary PtRhAu catalysts that selectively catalyze the hydrogenation of lignin-derived bio-oil (i.e. guaiacol), to the oxygenated chemicals (i.e. 2-methoxycyclohexanol), while suppressing deoxygenation. Density functional theory calculations suggests that the Pt catalysts modulated with Rh and Au steer the intermediate energetics to increase guaiacol coverage, foster hydrogenation, and suppress deoxygenation. Structural characterization, X-ray studies, *in-situ* Raman/infrared reflection-absorption spectroscopy (IRRAS), and electrochemical measurements further validate the role of Rh and Au in improving catalytic hydrogenation performance

and protecting oxygenated groups. We further achieved an integrated lignin biorefinery from birch wood to oxygenated chemical, indicating that PtRhAu electrocatalysts can selectively hydrogenate and funnel wood-derived lignin monomers to an oxygen-functionalized chemical with suppressed deoxygenation reaction. The strategy suggests a means to valorize biomass to oxygen-functionalized chemicals.

Methods

Computational details. All calculations were carried out using the Vienna ab-initio simulation program (VASP)[36,37]. Detailed theoretical methods can be found in Supplementary Information.

Catalyst synthesis. In a typical procedure, PtRhAu working electrode was synthesized by co-electrodepositing metals onto a Ti foam (1 x 1 cm^2) according to a slightly modified version of a previously reported method[38]. The electrodeposition was conducted in a three-electrode electrochemical cell using a potentiostat (Metrohm-Autolab, PGSTAT204). Carbon paper and an Ag/AgCl electrode (saturated with KCl) were used as the counter and reference electrodes, respectively. The substrate was subjected to 50 cycles of cyclic voltammetric scans in the range of potential between -0.5 to 1.7 V at a scan rate of 0.1 $V{\cdot}s^{-1}$. The electrolyte consisted of an aqueous solution of 0.5 M Na_2SO_4 containing 7 mM of H_2PtCl_6, 3 mM of $HAuCl_4$, and 4 mM of $Rh(NO_3)_3$. The Pt, Au, Rh, Ru, Ir, Pd, and Ag were synthesized by the similar procedure in the electrolyte containing 0.5 M Na_2SO_4 and 10 mM of metal precursor as needed. The optimized PtRh was synthesized using an electrolyte containing 0.5 M Na_2SO_4, 7 mM of H_2PtCl_6, and 4 mM of $Rh(NO_3)_3$. The optimized PtAu was synthesized using an electrolyte containing 0.5 M Na_2SO_4, 7 mM of H_2PtCl_6, and 3 mM of $HAuCl_4$. After the electrodeposition, the working electrode was rinsed with D.I. water and dried at atmospheric pressure and temperature.

Synthesis of control electrocatalysts. The nickel and copper foam were washed with methanol and D.I. water for three times and used as control catalysts. The other working electrodes based on other elements (Rh, Au, Ru, Ir, Pd, Ag) were synthesized by electrodepositing metals onto a Ti foam (1x1 cm^2) according to the slightly modified version of a previously reported method[38]. The electrodeposition was conducted in a three-electrode electrochemical cell using a potentiostat (Metrohm-Autolab, PGSTAT204). Carbon paper and an Ag/AgCl electrode (saturated with KCl) were used as the counter and reference electrodes, respectively. The electrolyte consisted of an aqueous solution of 0.5 M Na_2SO_4 containing 10 mM of metal precursor solution as needed. After the electrodeposition with 50 cycles of cyclic voltammetric scans in the range of potential between -0.5 and 1.7 V at a scan rate of 0.1 $V{\cdot}s^{-1}$, the working electrode was washed with D.I. water and dried in ambient pressure and temperature.

Materials characterization. The morphology of the electrodes was characterized using transmission electron microscopy (TEM, Hitachi HF-3300) and scanning transmission electron microscopy (STEM, FEI Titan 80-300 HB) equipped with an electron energy loss spectroscopy (EELS) detector. The crystal structures were determined using synchrotron X-ray diffraction analysis (the incident X-ray wavelength of 0.6909 Å), equipped with a large Debye-Scherrer camera in the BL-12B2 beamline (Spring-8, National

Synchrotron Radiation Research Center (NSRRC), Japan) in which the electron storage ring was operating at 8.0 GeV. The catalysts were deposited on carbon papers to collect the XRD patterns. The XRD patterns were calibrated using CeO_2 standard and modulated to that with a wavelength of 1.5413 Å using the software referred to as "Winplotr". In-situ X-ray absorption spectroscopy (XAS) were collected using the 9BM beamline of the Advanced Photon Source (Argonne National Laboratory, IL, United States). In-situ Raman spectroscopy was conducted using a Renishaw in Via Raman microscope, equipped with a 785 nm laser.

Electrochemical performance and product analysis. Electrocatalytic measurements were conducted in a three-electrode system equipped with Pt as counter electrodes using an electrochemical station (Metrohm-Autolab, PGSTAT204). All potentials were measured against an Ag/AgCl reference electrode (saturated KCl, BASi) and converted to the RHE reference scale using the following equation:

$$\text{E (vs RHE)} = \text{E (vs Ag/AgCl)} + 0.197\ \text{V} + 0.0591 \times \text{pH} \qquad (1)$$

Linear sweep voltammetry (LSV) measurements were performed by scanning the potential in the negative direction at a scan rate of 5 $mV \cdot s^{-1}$, while the electrolyte was magnetically stirred at 1000 RPM. The ECH of the lignin monomer was conducted using a two-chambered H-cell with Nafion 117 membrane as the separator. All working electrodes had a geometric surface area of 1 cm^2. 20 mL of 0.2 M $HClO_4$ containing 120 mM guaiacol was used as the electrolyte in cathode. We also performed bulk ECH of guaiacol using PtRhAu catalyst in 1 L of electrolyte for a continuous reaction of 12 hours.

The liquid products were quantified using a gas chromatography-mass spectra (GC-MS) (PerkinElmer Clarus 680) equipped with a Stabilwax column (fused silica, Restek) and a 700 MHz Agilent DD2 nuclear magnetic resonance (NMR) spectrometer. 4-propyl-cyclohexanone was used as the internal standard. Prior to the product analysis using GC-MS, 900 uL of electrolyte solution was collected from the reaction solution and extracted with 300 uL of dichloromethane. For NMR characterizations, 3 mL of electrolyte solution was extracted with 1 mL of chloroform-D. The faradaic efficiency (FE) toward 2MC was calculated using the following equation:

$$FE_{2MC} = \frac{6 \times n_{2MC} \times F}{I \times t} \qquad (2)$$

where n_{2MC} is the total amount of 2MC (in moles), F is the faradaic constant, I (in amperes) is the current, and t (in seconds) is the time for the constant current.

Upgrading birch wood to lignin monomer oils. Detailed experimental methods are in Supplementary Information.

Electrocatalytic hydrogenation of wood-derived lignin monomers. The ECH of the wood-derived lignin monomers was conducted using a two-chambered H-cell with Nafion 117 membrane as the separator. All working electrodes (PtRhAu deposited on carbon felt) had a geometric surface area of 1 cm^2. 20 mL of 0.2 M $HClO_4$ containing 6 mM lignin monomers mixture (4.8 mM 4PS and 1.2 mM 4PG) was used as the catholyte. The liquid products were quantified using the gas GC-MS (PerkinElmer Clarus 680) by following the similar procedure described previously. The liquid products were further characterized using 700 MHz Agilent DD2 nuclear magnetic resonance (NMR) spectrometer. The faradaic efficiency (FE) toward 2M4PC was calculated using the following equation:

$$FE_{2M4PC} = \frac{8 \times n_{2M4PC}}{I \times t} \times \frac{\text{moles of 4PS consumed}}{\text{moles of 4PS and 4PG consumed}} + \frac{6 \times n_{2M4PC}}{I \times t} \times \frac{\text{moles of 4PG consumed}}{\text{moles of 4PS and 4PG consumed}} \quad (3)$$

where n_{2M4PC} is the total amount of 2M4PC that is 2-methoxy-4-propylcyclohexanol (in moles), I (in amperes) is the current, t (in seconds) is the duration for the constant current applied, C_{4PS} is the conversion of 4PS, and C_{4PG} is the conversion of 4PG.

The overall conversion rate of lignin monomer oil was calculated using the following equation:

$$C_{overall} = \frac{\text{moles of 4PS and 4PG consumed}}{\text{initial moles of 4PS and 4PG}} \times 100\% \quad (4)$$

Declarations

Additional details. More sample characterizations as well as the computational simulation details are provided in the Supplementary Information.

Author contributions:

E.H.S., W.Z., and J.S.L. supervised this project. T.P. and T.Z. carried out catalyst design and synthesis. T.P. performed the electrochemical and GC-MS experiments. Y.Y. carried out in-situ Raman experiments, SEM, and electrochemical experiments. J.Q. carried out DFT calculations. G.R.D. and J.B.d.B. produced lignin monomer mixture from wood. S.H. assisted in synchrotron XRD experiments. S.H. and J.A. performed XAS characterization and data processing. J.W. and A.S. conducted the XPS measurements. G.L. assisted in preparing the carbon paper and H-Cell. M.W. carried out the ICP-AES experiments. D.H., Z.W., and B.C. performed the HRTEM experiments. Z.L. and L.S. carried out the IRRAS experiments. T.P., T.Z., W.Z., and E.H.S. wrote the manuscript. J.B.d.B., G.R.D., A.O., and F.P.G.d.A. provided help in manuscript writing. All authors discussed the results, helped in data analysis, and assisted in manuscript preparation.

Competing interests:

The authors declare no competing interests.

Acknowledgements

The authors thank Cathleen Crudden from Queen's University and Dr. Yuguang C. Li from University of Toronto for fruitful discussions. The authors thank Y.-F. Liao for the technical support of synchrotron XRD at the BL-12B2 beamline at SPring-8 (NSRRC). The authors thank N. Hamada from the Canadian Centre for Electron Microscopy (CCEM), Brockhouse Institute for Materials Research, McMaster University for the STEM and EELS measurement support.

Funding: This work was supported by the Ontario Research Fund: Research Excellence Program, the Natural Sciences and Engineering Research Council (NSERC) of Canada, the CIFAR Bio-Inspired Solar Energy program. All DFT computations were performed on the IBM BlueGene/Q supercomputer with support from the Southern Ontario Smart Computing Innovation Platform (SOSCIP) funded by the Federal Economic Development Agency of Southern Ontario, the Province of Ontario, IBM Canada Ltd., Ontario Centres of Excellence, Mitacs and 15 Ontario academic member institutions. This research is partially supported by Compute Ontario (www.computeontario. ca) and Compute Canada (www.computecanada.ca). This work was partially supported by the Natural Science Foundation of China (21972096) and the Shenzhen Science and Technology Program (JCYJ20190808150615285). The authors thank D. M. Meira for XAS experiments at the Advanced Photon Source (APS), which is an Office of Science User Facility operated for the U.S. Department of Energy (DOE) Office of Science by Argonne National Laboratory, and was supported by the U.S. DOE under Contract No. DE-AC02-06CH11357, and the Canadian Light Source and its funding partners. The IRRAS experiment was carried out at Brookhaven National Laboratory supported by the U.S. Department of Energy, Office of Science, Office of Basic Energy Sciences (BES), Chemical Sciences, Geosciences and Biosciences Division under contract DE-SC0012704.

References

1 Sanderson, K. Lignocellulose: A chewy problem. *Nature* **474**, S12-14 (2011).

2 Schutyser, W. *et al.* Chemicals from lignin: An interplay of lignocellulose fractionation, depolymerisation, and upgrading. *Chem. Soc. Rev.* **47**, 852-908 (2018).

3 Ragauskas, A. J. *et al.* Lignin valorization: Improving lignin processing in the biorefinery. *Science* **344**, 1246843 (2014).

4 Sun, Z. *et al.* Complete lignocellulose conversion with integrated catalyst recycling yielding valuable aromatics and fuels. *Nat. Catal.* **1**, 82-92 (2018).

5 Shuai, L. *et al.* Formaldehyde stabilization facilitates lignin monomer production during biomass depolymerization. *Science* **354**, 329-333 (2016).

6 Xiao, D. J. *et al.* A closed cycle for esterifying aromatic hydrocarbons with CO_2 and alcohol. *Nat. Chem.* **11**, 940-947 (2019).

7 Bondue, C. J., Calle-Vallejo, F., Figueiredo, M. C. & Koper, M. T. M. Structural principles to steer the selectivity of the electrocatalytic reduction of aliphatic ketones on platinum. *Nat. Catal.* **2**, 243-250 (2019).

8 Cha, H. G. & Choi, K. S. Combined biomass valorization and hydrogen production in a photoelectrochemical cell. *Nat. Chem.* **7**, 328-333 (2015).

9 Awad, O. I. *et al.* Overview of the oxygenated fuels in spark ignition engine: Environmental and performance. *Renew. Sust. Energ. Rev.* **91**, 394-408 (2018).

10 Meyers, J. *et al.* Electrochemical conversion of a bio-derivable hydroxy acid to a drop-in oxygenate diesel fuel. *Energy Environ. Sci.* **12**, 2406-2411 (2019).

11 Jin, W. *et al.* Catalytic upgrading of biomass model compounds: Novel approaches and lessons learnt from traditional hydrodeoxygenation - a review. *ChemCatChem* **11**, 924-960 (2019).

12 Liu, H., Jiang, T., Han, B., Liang, S. & Zhou, Y. Selective phenol hydrogenation to cyclohexanone over a dual supported Pd-Lewis acid catalyst. *Science* **326**, 1250-1252 (2009).

13 Liu, W. *et al.* Ambient-pressure and low-temperature upgrading of lignin bio-oil to hydrocarbons using a hydrogen buffer catalytic system. *Nature Energy* **5**, 759-767 (2020).

14 Shim, J.-O. *et al.* Facile production of biofuel via solvent-free deoxygenation of oleic acid using a CoMo catalyst. *Appl. Catal., B Environ.* **239**, 644-653 (2018).

15 Pattanaik, B. P. & Misra, R. D. Effect of reaction pathway and operating parameters on the deoxygenation of vegetable oils to produce diesel range hydrocarbon fuels: A review. *Renew. Sust. Energ. Rev.* **73**, 545-557 (2017).

16 Peters, B. K. *et al.* Scalable and safe synthetic organic electroreduction inspired by Li-ion battery chemistry. *Science* **363**, 838-845 (2019).

17 Liao, Y. *et al.* A sustainable wood biorefinery for low–carbon footprint chemicals production. *Science* **367**, 1385, doi:10.1126/science.aau1567 (2020).

18 Zeng, L. *et al.* Electrochemical oxidative aminocarbonyl of terminal alkynes. *Nat. Catal.* (2020).

19 Cao, Z., Dierks, M., Clough, M. T., Daltro de Castro, I. B. & Rinaldi, R. A convergent approach for a deep converting lignin-first biorefinery rendering high-energy-density drop-in fuels. *Joule* **2**, 1118-1133 (2018).

20 Liao, Y. *et al.* A sustainable wood biorefinery for low-carbon footprint chemicals production. *Science* **367**, 1385-1390 (2020).

21 Mohle, S. *et al.* Modern electrochemical aspects for the synthesis of value-added organic products. *Angew. Chem. Int. Ed. Engl.* **57**, 6018-6041 (2018).

22 Carneiro, J. & Nikolla, E. Electrochemical conversion of biomass-based oxygenated compounds. *Annu. Rev. Chem. Biomol. Eng.* **10**, 85-104 (2019).

23 Lee, I., Delbecq, F., Morales, R., Albiter, M. A. & Zaera, F. Tuning selectivity in catalysis by controlling particle shape. *Nat. Mater.* **8**, 132-138 (2009).

24 James, O. O., Sauter, W. & Schröder, U. Electrochemistry for the generation of renewable chemicals: One-pot electrochemical deoxygenation of xylose to δ-valerolactone. *ChemSusChem.* **10**, 2015-2022 (2017).

25 Chen, G. *et al.* Interfacial electronic effects control the reaction selectivity of platinum catalysts. *Nat. Mater.* **15**, 564-569 (2016).

26 Truppo, M. D. *Biocatalysis in the pharmaceutical and biotechnology industries*. Vol. 11 (American Chemical Society, 2007).

27 Schumann, W. K., Kut, O. M. & Baiker, A. Influence of reaction parameters on the stereoselectivity of the nickel-catalyzed gas-phase hydrogenation of o-cresol. 1. Kinetics and reaction pathway. *Ind. Eng. Chem. Res.* **28**, 693-697 (1989).

28 Talebi Amiri, M., Dick, G. R., Questell-Santiago, Y. M. & Luterbacher, J. S. Fractionation of lignocellulosic biomass to produce uncondensed aldehyde-stabilized lignin. *Nat Protoc* **14**, 921-954, doi:10.1038/s41596-018-0121-7 (2019).

29 Li, Z. *et al.* Mild electrocatalytic hydrogenation and hydrodeoxygenation of bio-oil derived phenolic compounds using ruthenium supported on activated carbon cloth. *Green Chem.* **14**, 2540-2549 (2012).

30 Bond, G. C. *Metal-catalysed reactions of hydrocarbons*. (Springer, 2005).

31 Almeida, C. V. S. *et al.* Highly active Pt_3Rh/C nanoparticles towards ethanol electrooxidation. influence of the catalyst structure. *Appl. Catal., B Environ.* **254**, 113-127 (2019).

32 Agarwal, U. P., McSweeny, J. D. & Ralph, S. A. FT–Raman investigation of milled-wood lignins: Softwood, hardwood, and chemically modified black spruce lignins. *J. Wood Chem. Technol.* **31**, 324-344

(2011).

33 Verma, V. N., Nair, K. P. R. & Rai, D. K. Vibrational spectra and thermodynamic functions of the three isomeric methoxyphenols. *Isr. J. Chem.* **8**, 777-789 (1970).

34 Neelakantan, P. The Raman spectrum of cyclohexanol. *Proc. Ind. Acad. Sci., A* **57**, 94-102 (1963).

35 Abu-Omar, M. M. *et al.* Guidelines for performing lignin-first biorefining. *Energy Environ. Sci.*, doi:10.1039/d0ee02870c (2020).

36 Kresse, G. & Furthmüller, J. Efficient iterative schemes for ab initio total-energy calculations using a plane-wave basis set. *Phys. Rev. B* **54**, 11169-11186 (1996).

37 Kresse, G. & Furthmüller, J. Efficiency of ab-initio total energy calculations for metals and semiconductors using a plane-wave basis set. *Comput. Mater. Sci.* **6**, 15-50 (1996).

38 Kloke, A., Kohler, C., Gerwig, R., Zengerle, R. & Kerzenmacher, S. Cyclic electrodeposition of PtCu alloy: Facile fabrication of highly porous platinum electrodes. *Adv. Mater.* **24**, 2916-2921 (2012).

Figures

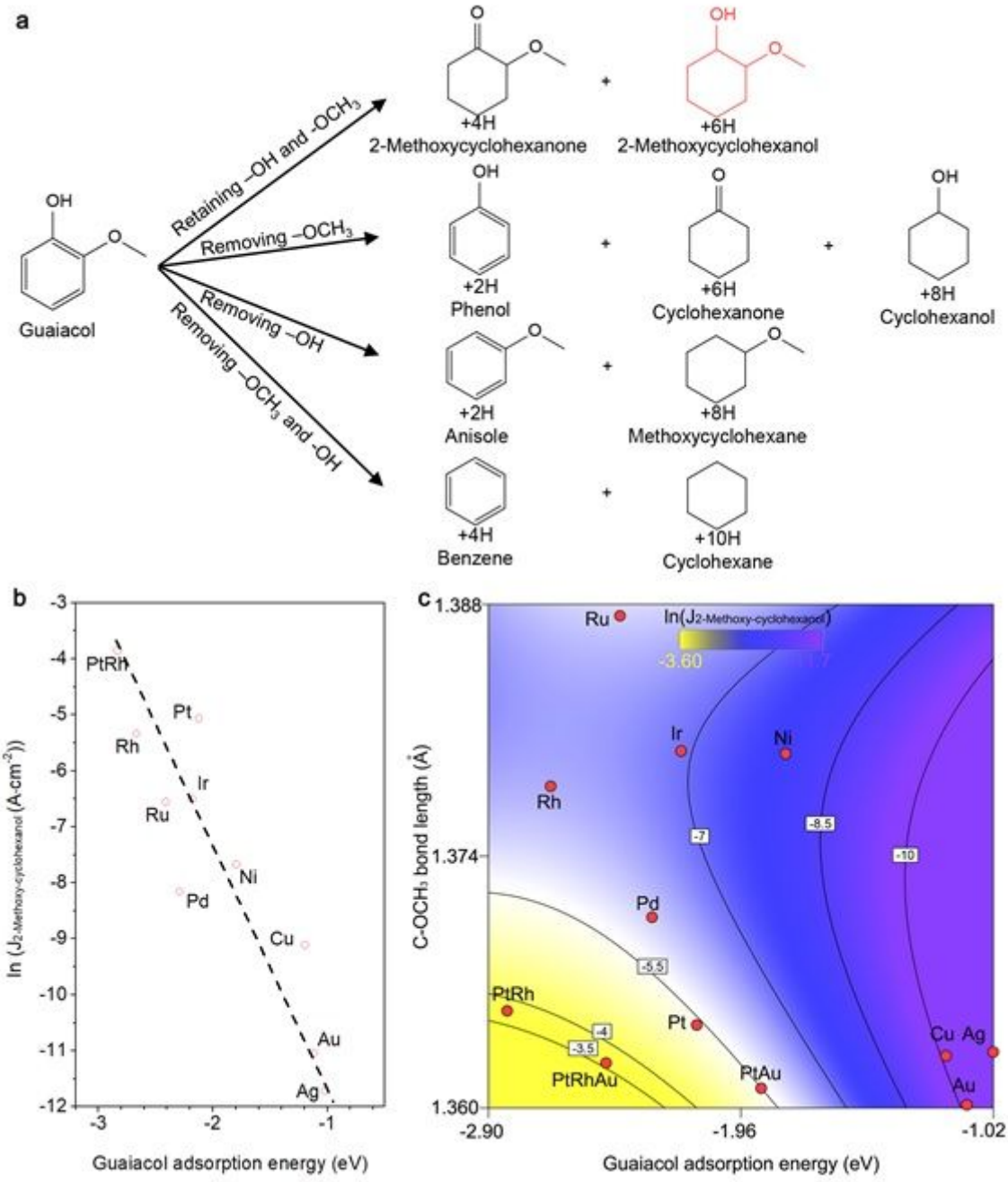

Figure 1

Steering catalyst activity and selectivity toward 2-methoxycyclohexanol by tuning guaiacol adsorption energy and C-OCH3 bond length. a, Electrocatalytic hydrogenation of guaiacol and potential products. 2-methoxycyclohexanol is the target structure in red. b, Correlation between guaiacol adsorption energy and electrocatalytic hydrogenation performance (ln(J2-Methoxycyclohexanol)). c, Interaction between guaiacol adsorption energy and C-OCH3 bond length on electrocatalytic hydrogenation performance (ln(J2-Methoxycyclohexanol)).

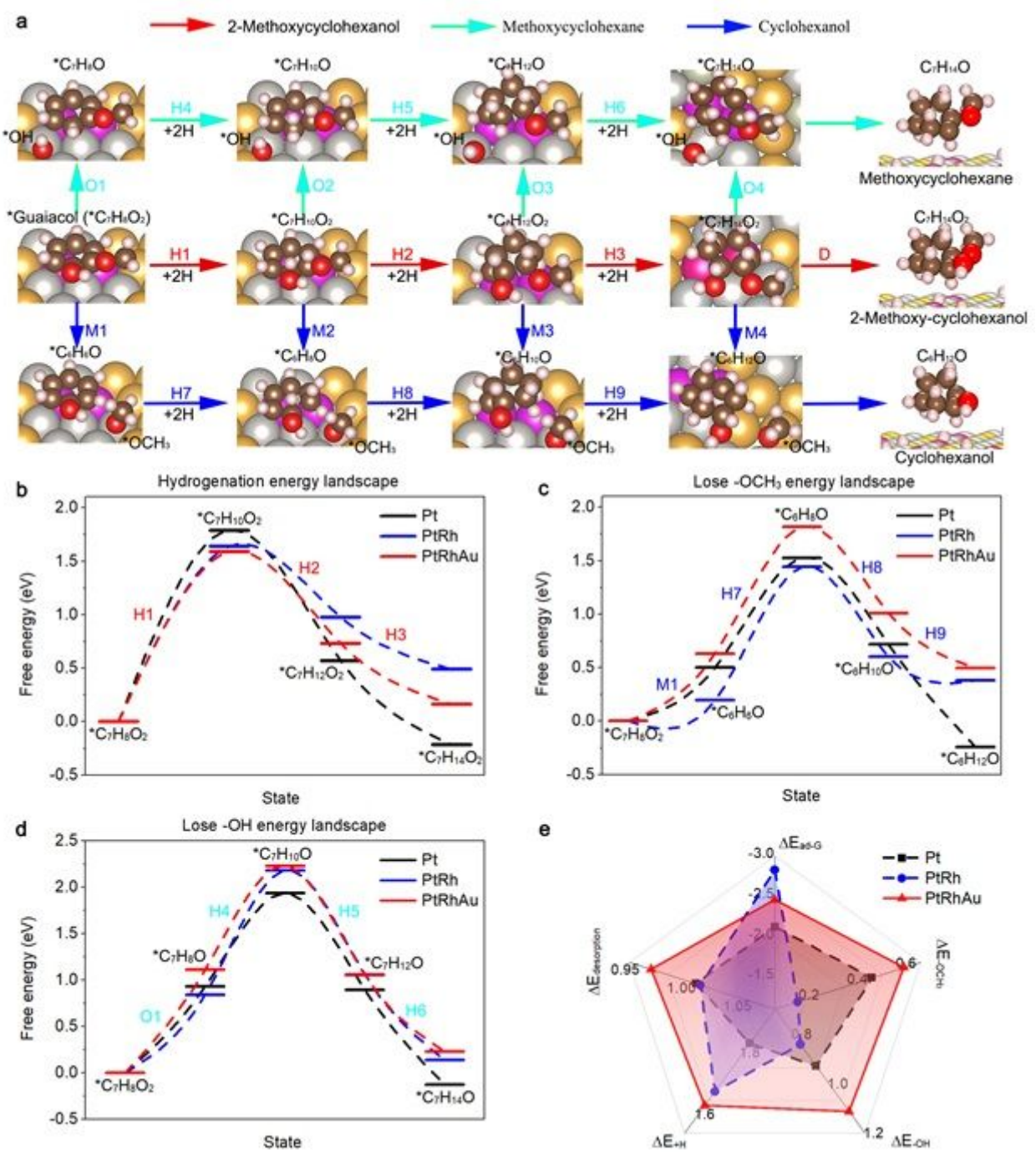

Figure 2

DFT calculations on 2-methoxy-cyclohexanol formation. a, Geometries of reactant and intermediates on PtRhAu catalyst surface for the formation of 2-methoxycyclohexanol and two main competing reactions. The reaction pathway to 2-methoxycyclohexanol: H1, addition of the first hydrogen pairs to guaiacol adsorbed onto catalyst surface, H2, addition of the second hydrogen pairs, H3, addition of the third hydrogen pairs, D, desorption. The competing reaction steps O1-O4, M1-M4, and H4-H9 represent dihydroxylation, demethoxylation, and hydrogenation respectively. Grey, yellow, purple, brown, red, and pink balls represent Pt, Au, Rh, C, O, and H atoms, respectively. b, Free energy profiles for electrocatalytic hydrogenation of guaiacol to 2-methoxycyclohexanol pathway H1-H3 as illustrated in (a). c, Free energy

profiles for demethoxylation pathway M1-H7-H8-H9 as illustrated in (a). d, Free energy profiles for dehydroxylation steps O1-H4-H5-H6 as illustrated in (a). e, Comparison of five elementary steps and selectivity for catalysts. ΔEad-G represents the guaiacol adsorption energy. ΔE-OCH3, ΔE-OH, ΔE+H and ΔEdesorption represent the energy difference for losing -OCH3 in the step M1, losing -OH in the step O1, electrocatalytic hydrogenation in step H1 and desorption in step D as illustrated in (a).

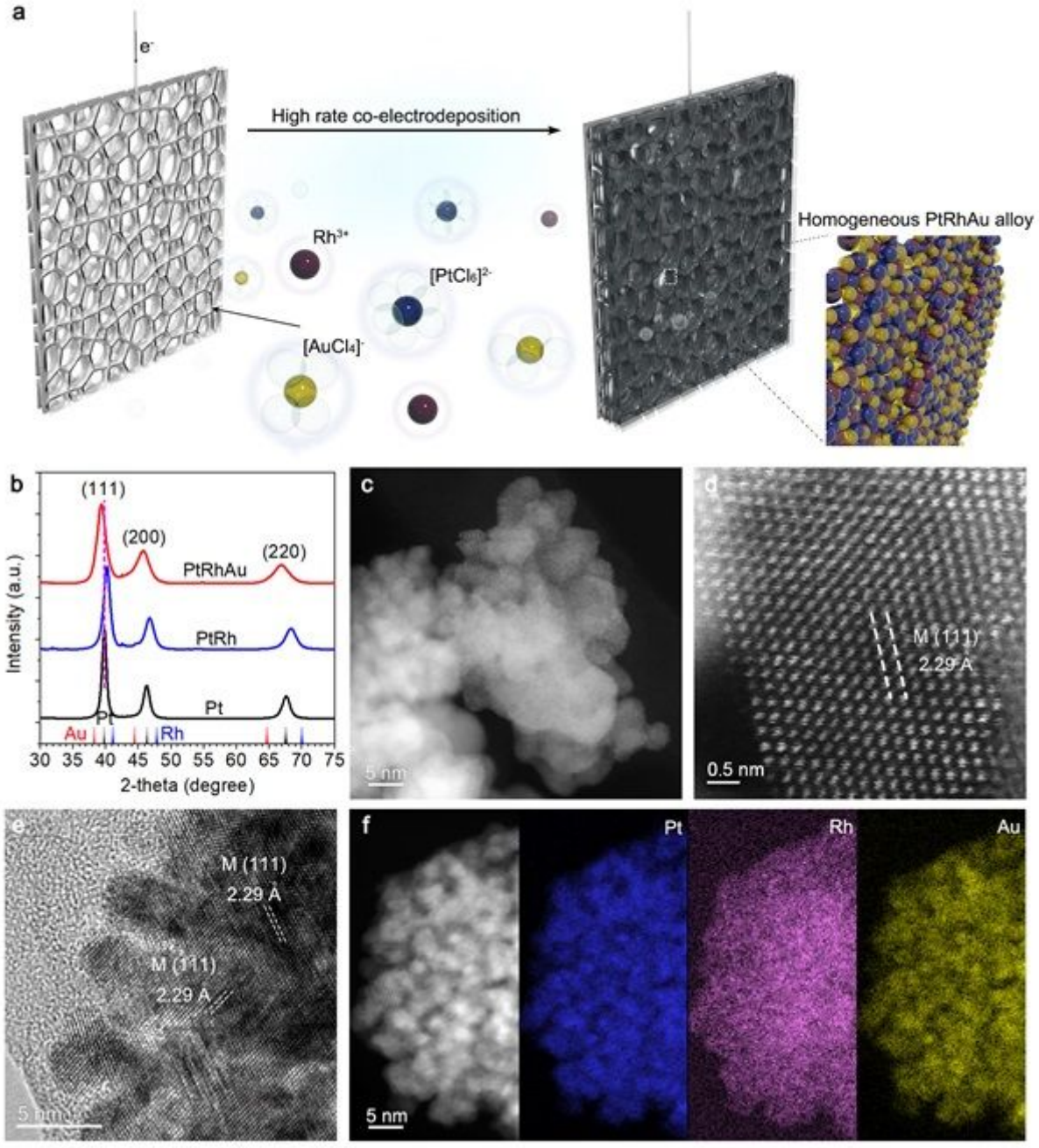

Figure 3

Catalyst design and structural characterization. a, Schematic illustrating the fabrication of PtRhAu catalysts coating on titanium foam. b, Synchrotron XRD spectra of Pt, PtRh, and PhRhAu samples, showing the peak shift and the alloy structure. c-e, STEM (c and d) and HRTEM (e) images of PtRhAu

nanoparticles, showing the dendritic morphology and the lattice spacing. f, EELS of PtRhAu indicating the homogeneous distribution of Pt, Au, and Rh elements.

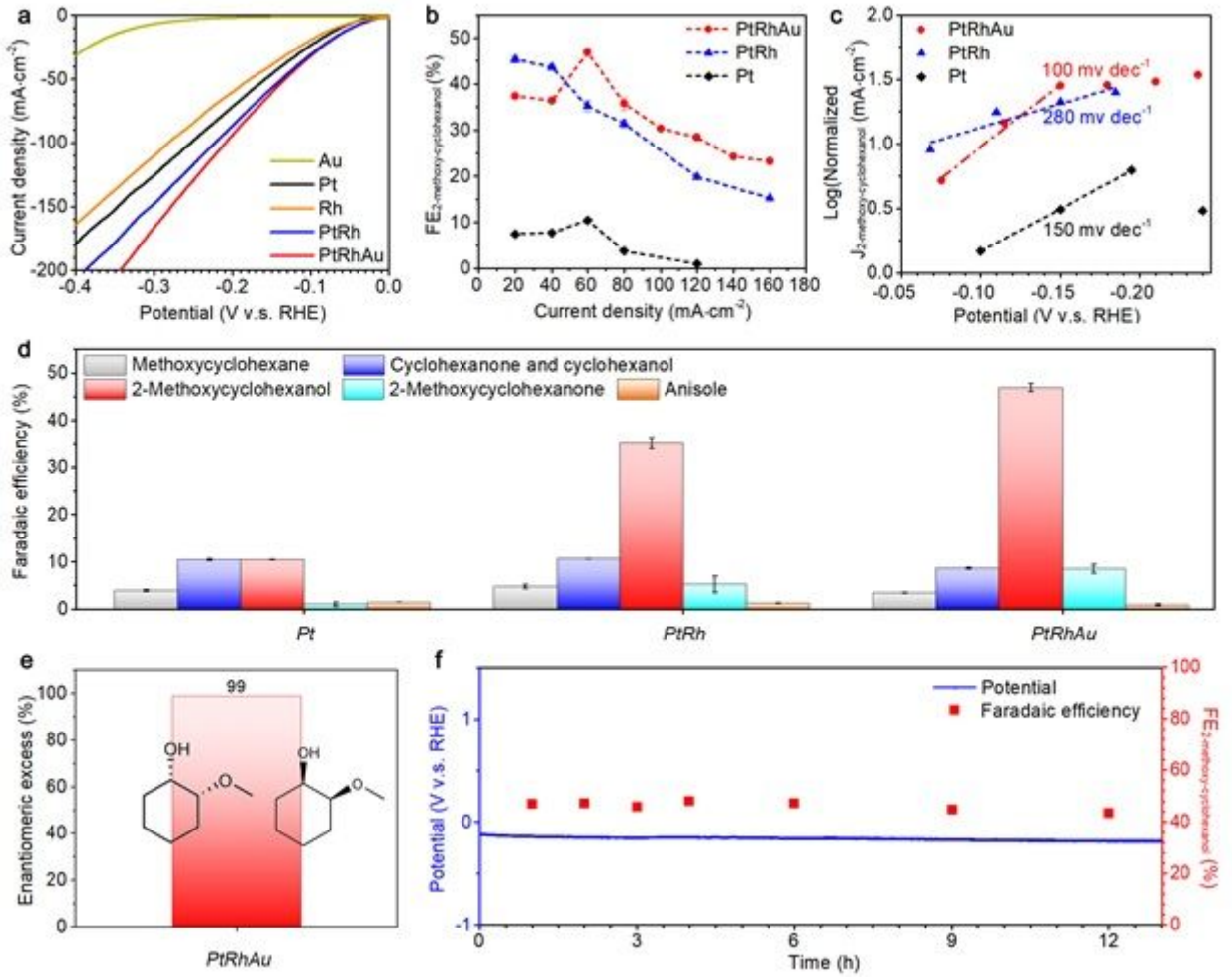

Figure 4

Guaiacol electrocatalytic hydrogenation (ECH). a, Linear sweep voltammetry curves in an aqueous electrolyte containing 120 mM guaiacol and 0.2 M HClO4. b, Faradaic efficiency toward 2-methoxycyclohexanol at various current densities for 1 hour. c, Partial current densities toward 2-methoxycyclohexanol and Tafel slope for selected catalysts. d, Faradaic efficiency toward 2-methoxycyclohexanol on various catalysts at 60 mA·cm-2. e, Selective toward cis-2-methoxycyclohexanol. f, Stable chronoamperometric operation of PtRhAu at a current density of 60 mA·cm-2 with the optimum faradaic efficiency toward 2-methoxycyclohexanol.

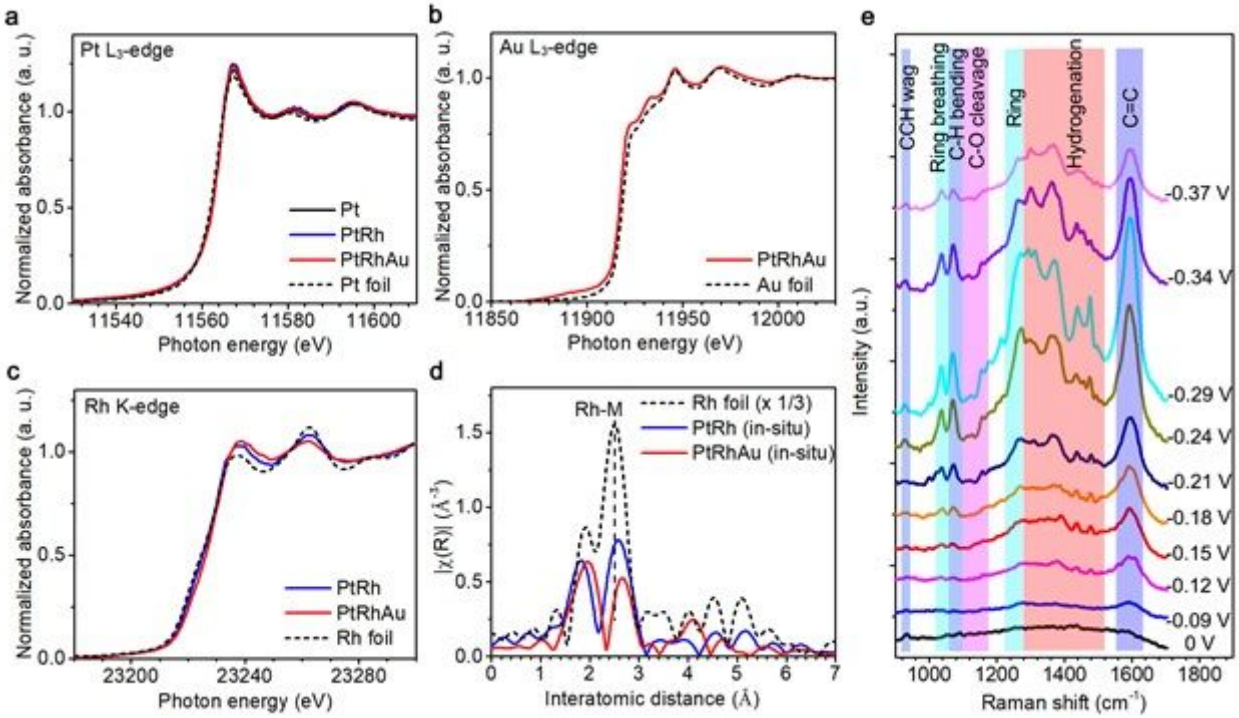

Figure 5

XAS and operando Raman spectra. a-c, (a) Pt L3-edge, (b) Au L3-edge, and (c) Rh K-edge XAS of pristine PtRhAu, PtRh, and Rh foil standard. d, EXAFS investigation into the local atomic structure around Rh atoms. e, In-situ Raman spectra of the electrocatalytic hydrogenation of guaiacol on PtRhAu catalyst in 0.2 M electrolyte with 120 mM guaiacol.

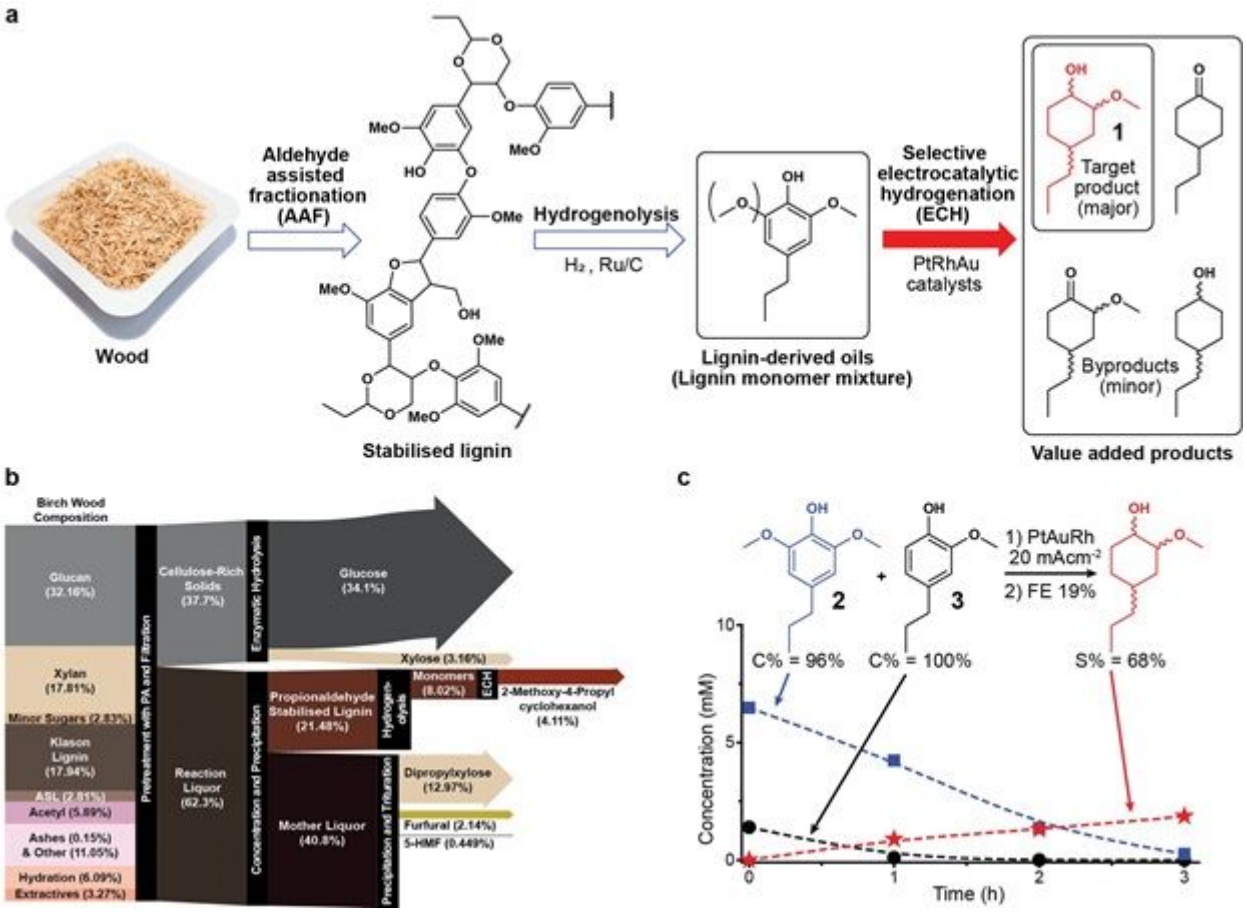

Figure 6

Integrated lignin valorization from birch wood to an oxygenated product 2-methoxy-4-propylcyclohexanol. a, Integrated lignin valorization process for high-value 2-methoxy-4-propylcyclohexanol from birch wood. 2-methoxy-4-propylcyclohexanol (1, red) is the target structure in bold. b, Mass balances during the propionaldehyde assisted fractionation of lignocellulosic biomass, as performed on birch wood. All the numbers are provided as weight percentages. The provided weight percentages of the sugars, stabilized sugars, furfural, hydroxymethylfurfural (5-HMF), stabilized lignin, and lignin monomers have been corrected for the mass of the stabilizing group, hydration, dehydration, or hydrogenation, to match their initial structure in the native biomass. Abbreviations: hydroxymethylfufural (HMF), acid soluble lignin (ASL). c, Concentration evolution of lignin monomer mixture containing 4-propylguaiacol (2, blue) and 4-propylguaiacol (3, black) and target product 2-methoxy-4proplycyclohexanol (1, red) over 3 hours. (Inset) Electrocatalytic hydrogenation on PtRhAu catalyst at a current density of 20 mA·cm-2, showing the faradaic efficiency (FE) at 1 hour, conversion rate (C%), and product selectivity (S%) after 3 hours of reaction.

Supplementary Files

This is a list of supplementary files associated with this preprint. Click to download.

- SIPtRhAuelectrocatalyticbiorefinary.docx